Materials Advances

ROYAL SOCIETY OF CHEMISTRY

PAPER

View Article Online
View Journal | View Issue

Cite this: *Mater. Adv.*, 2024, 5, 2128

pH-sensitive composite nanofibers of poly(ε-caprolactone) loaded with iron oxide nanoparticles/ammonium bicarbonate as a nanocarrier toward efficient doxorubicin release for postsurgical cancer treatment†

Quang Nhat Quynh Vo,‡[a] Abdelrahman I. Rezk,‡[abc] Sungkun Chun,*[bc] Chan Hee Park*[ad] and Cheol Sang Kim*[ad]

The concurrent use of hyperthermia and chemotherapy has attracted considerable interest in the *in situ* treatment of cancer after surgical resection. In this study, poly(ε-caprolactone) (PCL) is embedded with iron oxide nanoparticles (IONPs) and ammonium bicarbonate pH-responsive moieties that conjugate with the DOX anticancer drug incorporated into the core of nanofibers. The synthesized composite nanofibers were characterized using FESEM, EDS, FTIR, and XRD analyses. The composite nanofibers display a temperature increase in a concentration dependant manner with IONPs using an FLIR camera under AMF excitation. The main advantage of our scaffold is that it can be directly implanted in the tumor site, thus ensuring high IONP loading and higher magnetic response. When exposed to the characteristic acidic pH of tumor tissues, the ammonium bicarbonate pH-responsive moieties dissociate, releasing the DOX, and intelligently convert the pH-triggered drug release into a tumor-triggered drug release. Simultaneously, the hyperthermal capability of the IONPs in the nanofibers, generated by applying an alternating magnetic field (AMF), results in localized heating of the tumor tissues and hence synergistic tumoricidal activities. *In vitro* cytotoxicity experiments further confirmed that PIAD composite nanofiber mats showed an enhanced inhibitory effect against MCF7 cells by the combination of hyperthermia and chemotherapy. Therefore, the magnetic polymeric nanofibers produced by electrospinning provide a promising controlled drug delivery nanosystem for postsurgical breast cancer treatment.

Received 19th November 2023,
Accepted 8th January 2024

DOI: 10.1039/d3ma01026k

rsc.li/materials-advances

1. Introduction

In spite of continuous progress in medical research, breast cancer persists as the most common form of cancer, estimated to be the leading cause of new cases and deaths among women in 2023. Cancer remains one of the most challenging health problems worldwide, with over 19 million new cases and almost 10 million deaths reported annually.[1] Conventional chemotherapy, the most common approach for cancer treatment, is often associated with significant side effects due to the non-specific nature of the drugs used, which can lead to toxicity and reduced efficacy.[2,3] Despite the advancements in postsurgical therapy and chemotherapy, the therapeutic treatment remains of significant concern. The risk of local recurrence is high in the cases that have been treated with breast-preserving surgery (lumpectomy), compared with those treated with resection surgery (mastectomy); nevertheless, radiotherapy is able to noticeably decrease the frequency of cancer recurrence. Therefore, it is necessary to design an implantable scaffold for localized drug delivery and good obliteration of the residual tumor cells, thereby impeding local cancer recurrence.

In recent years, various strategies have been explored to improve the effectiveness of cancer treatment while reducing

[a] *Department of Bionanotechnology and Bioconvergence Engineering, Graduate School, Jeonbuk National University, Jeonju 561–756, Republic of Korea. E-mail: chskim@jbnu.ac.kr, biochan@jbnu.ac.kr; Fax: +82 63 270 2460; Tel: +82 63 270 4284*
[b] *Department of Physiology, Jeonbuk National University Medical School, Jeonju-si 54907, Republic of Korea. E-mail: sungkun.chun@jbnu.ac.kr*
[c] *BK21FOUR 21st Century Medical Science Creative Human Resource Development Center, Republic of Korea*
[d] *Mechanical Design Engineering, Jeonbuk National University, Jeonju 561–756, Republic of Korea*

† Electronic supplementary information (ESI) available. See DOI: https://doi.org/10.1039/d3ma01026k

‡ Quang Nhat Quynh Vo and Abdelrahman I. Rezk contributed equally to this work.

the side effects, including the development of nanotechnology-based drug delivery systems.[4–6] Different polymer-based drug carriers, including polymeric nanoparticles, nanocapsules, liposomes, hydrogels, micelles, solid lipid nanoparticles, nanoemulsions, and nanofibers, have been studied as implantable drug delivery devices.[7–9] Among them, the nanofibrous scaffolds prepared by the electrospinning process, due to their high surface area, porous structure and higher drug loading capability, have been extensively used for the controlled release of anticancer drugs.[10–14]

pH-sensitive magnetic nanofibers have emerged as a promising platform for controlled drug delivery due to their unique properties, which include magnetic responsiveness and pH sensitivity.[12,15,16] The magnetic nanoparticles enable the nanofibers to be guided to a specific site in the body using an external magnetic field, while the pH-responsive moieties allow for targeted drug release at a specific pH value, such as the slightly acidic environment found in cancer cells.[15]

By allowing for localized drug delivery, minimizing off-target effects, and reducing the required dosage of drugs, this technology has the potential to improve the efficacy and reduce the toxicity of chemotherapy.[16]

Through the use of pH-sensitive magnetic nanofibers, drugs can be directly implanted into the tumor site, ensuring that only the affected cells are exposed to the therapeutic agent, while healthy cells are spared.[16] Additionally, the magnetic properties of the nanofibers enable the use of non-invasive techniques, such as magnetic resonance imaging (MRI), to monitor their distribution and accumulation in the targeted area, further enhancing the precision of drug delivery. Therefore, the use of pH-sensitive magnetic nanofibers is not limited to drug delivery alone, as they can also be utilized for cancer diagnosis.

Hyperthermia, the selective heating of tumor cells, is a well-established method for cancer treatment, which is employed based on evidence indicating that cancer cells are more sensitive than normal cells to the high temperatures of 43–45 °C,[17–20] and can be achieved through the use of magnetic nanoparticles.[15] When subjected to an alternating magnetic field, magnetic nanoparticles generate heat, which can be used to destroy cancer cells. By incorporating magnetic nanoparticles into pH-sensitive nanofibers, hyperthermia can be targeted specifically to cancer cells, while minimizing damage to healthy tissues. Hyperthermia can also enhance the effects of certain anticancer drugs, such as salinomycin,[21] curcumin,[22] paclitaxel (PTX),[15,23] and doxorubicin (DOX),[24,25] increasing the susceptibility of some cancer cells to these drugs.

Ammonium bicarbonate (NH_4HCO_3), which is usually used for the generation of gaseous bubbles in baked foods, has been actively considered for the development of drug release under both acidic and thermal conditions due to its decomposition, and like carbon dioxide (CO_2), bicarbonate ions are also easily discharged through the lungs, implying potential treatment safety, subsequently creating permeable defects in drug delivery systems. In addition, ammonia (NH_3) and ammonium ions (NH_4^+) are also the common metabolites in the human body and can be entirely removed from living organisms without hazardous effects.[26,27] Permeable defects can thus be created in the scaffold under acidic conditions similar to that found in the tumor microenvironment to induce rapid DOX release and further locally increase the drug concentration to obtain improved therapeutic results. In this study, we present pH-sensitive magnetic nanofibers for controlled drug delivery and potential postsurgical cancer therapy. We discuss the various design strategies used to optimize their performance, and their physicochemical and thermochemical features have been studied. In addition, we discuss *in vitro* studies evaluating their efficacy using MCF-7 cancer cells and the potential applications of these nanofibers in cancer treatment. Ultimately, the development of pH-sensitive magnetic nanofibers has the potential to significantly improve the outcomes of cancer treatment and enhance the quality of life of cancer patients.

2. Experimental

2.1. Materials

In this study, iron(II) sulfate heptahydrate, iron(III) chloride hexahydrate, poly(ε-caprolactone) (PCL, average M_w: 80 000), ammonium bicarbonate (NH_4HCO_3), ammonium hydroxide, and doxorubicin hydrochloride (DOX) were purchased from the Sigma-Aldrich Company (South Korea). Chloroform 99.5% (CH_3Cl), oleic acid, and *N*,*N*-dimethylformamide (DMF) were obtained from Samchun Pure Chemical, South Korea. The water employed in all experiments was treated using a Millipore Milli-Q purification system.

2.2. Preparation of iron oxide nanoparticles (IONPs)

Iron oxide nanoparticles were synthesized using a co-precipitation method derived from the literature. In brief, 5.4 g of $FeCl_3{\cdot}6H_2O$ and 2.8 g of $FeSO_4{\cdot}7H_2O$ were dissolved in 40 and 20 mL of distilled water, respectively, before being thoroughly mixed in a two-neck round flask, and magnetically stirred under nitrogen flow. IONPs were precipitated in a nitrogen atmosphere to prevent oxidation of the precursors and the product. Following that, the temperature of the solution was raised to 40 °C with stirring. The pH was adjusted by carefully adding 20 mL of NH_4OH (97%) drop-by-drop. The resulting suspension was vigorously stirred for 5 min. Following that, 1 mL of oleic acid was added to the solution dropwise. Next, the temperature of the mixture was raised to 80 °C and held for 20 min. To complete the process, the black–brown precipitates were cooled to room temperature by removing the heat source and then collected with a magnet. During the purification process, centrifugation with ethanol and distilled water was performed several times. The IONPs were dried overnight at a temperature of 70 °C.

2.3. Preparation of the PCL@IONPs@DOX@Ammonium bicarbonate (PIAD) and PCL@IONPs@Ammonium bicarbonate (PIA) electrospun fibers

First, PCL polymer solution was prepared by dissolving the blended solvent of DMF and chloroform ($CHCl_3$) at 10% (w/v) in

a 50 : 50 ratio. Following that, the different volumes of the NH_4HCO_3 saturated solution (0.005 and 0.01 mL) were added into the solvent at ambient temperature while being vigorously stirred for 30 min using a magnetic stirrer. DOX was then added and stirred for 30 min. To collect the homogenous solution, IONPs were lastly inserted and dispersed by ultrasonication for 15 min. After that, the blend solution was injected into a syringe pump that was connected to a high voltage apparatus. PIA was synthesized by the same method without DOX. Electrospinning was conducted using a high-voltage power supply at 18 kV, an infusion pump operating at a constant feed rate of 1 mL h^{-1}, and a 12 mL syringe fitted with a 21-gauge needle with a distance of 15 cm between the needle tip and collector and under environmental conditions of 35–40% humidity and 25–30 °C. A polyethylene sheet attached to the collector 15 cm from the needle tip was used to collect the electrospun fibers. The collector plate was an aluminum foil-wrapped negative electrode.

2.4. Characterization

The morphology and elemental composition of the surface functionalized fiber mats were investigated by scanning electron microscopy (SEM, Carl Zeiss supra-40 VP Germany). Incorporation of IONPs was ascertained by energy-dispersive X-ray spectroscopy (EDS) and transmission electron microscopy (TEM; JEOL, JEM-2010, Japan) imaging. Fourier transform infrared spectroscopy (FT-IR, PerkinElmer, Spectrum GX, USA) was used to characterize the bonding configurations of the electrospun mats. The scanning range was set to 380–4000 cm^{-1}. The ImageJ software (NIH, USA) was used to analyze the fiber diameter, where 100 fibers from different images of the corresponding samples were randomly selected to obtain the average fiber diameter. The crystallinity of the fiber mats was analyzed by X-ray diffractometry (XRD, Rigaku). Thermogravimetric analysis (TGA, Netzsch, TG 209 F3, Germany) was used to investigate the IONP concentration on the fiber mat. The sample weight was 10 mg. The samples were scanned from 30 to 600 °C at a rate of 10 °C min^{-1} and at a 50 mL min^{-1} flow rate of nitrogen atmosphere, to avoid oxidation of the samples. The magnetic properties of IONPs and IONPs incorporated into PCL fibers were investigated by VSM (Meghnatis Daghigh Kavir Co., Iran) at a magnetic field strength of ±15 kOe at RT. The cells were observed using an LSM510 confocal laser-scanning microscope (Carl Zeiss, Germany). The contact angle (wettability) was measured by using the deionized water contact angle measurement system, using a contact angle meter (Digidrop, GBX, France). Deionized water was automatically dropped (drop diameter 6 μm) onto the mat and measured at 1, 5, and 10 s.

2.5. Alternating magnetic field (AMF)-induced heating ability of PIA and IONPs

By applying an AMF using an appropriate generator (OSH-120-B, OSUNG HITECH, Republic of Korea) at RT, the heat generating capabilities of the IONPs and PIA were examined. PCL was the control sample. The intensity and frequency of the magnetic field were set to 12.57 kA m^{-1} and 293 kHz, respectively. In a typical procedure, 3 mg of IONPs was dissolved in 1 mL of deionized water and placed at the center of the coil. In the case of the nanofibers, the AMF was applied to 20, 40, and 60 mg of PIA positioned at the center of the coil. The temperature rise on different mats was monitored using a thermal camera (FLIR C-series thermal camera). The temperature was calibrated and maintained for 10 min before each experiment.

2.6. *In vitro* drug release

PCL–DOX (control sample), PIAD 0.5, and PIAD 1 drug release profiles were studied in PBS solution at pH = 7.4 and 5 and at 37 °C. An equal number of nanofiber membranes were weighed and placed in separate tubes containing 3 mL of PBS solution. All the samples for the release studies were incubated in a shaking incubator at 37 °C with a vibrating speed of 100 rpm. At predefined time intervals, 3 mL of the release solution (PBS) was removed from each tube and replaced with an equivalent volume of fresh PBS to keep the volume constant, and the quantity of DOX released was measured by recording the UV-vis absorption spectra at 480 nm. To ensure accuracy, experiments were carried out in triplicate for each sample. The amount of DOX released was determined using a calibration curve constructed from the known DOX concentration. The calibration curve fits Lambert and Beer's Law:

$$A = ac + b$$

where A is the absorbance, a is the slope, b is the intercept, and c is the drug concentration.

2.7. *In vitro* cell culture study

2.7.1. Biocompatibility study of nanofibers. Cell viability was evaluated using the CCK-8 test (Dojindo's cell counting kit–8) after 1, 3, and 5 days (d) of culture. In a 48-well plate, same-sized samples were prepared after being sterilized for 24 h under UV light. Before cell seeding, samples were rinsed with the medium and then washed with PBS. Nanofibers were taken in triplicate along with the control, which only had cells seeded onto the coverslip (SPL Lifesciences, Korea). In a pre-incubated Petri plate with the scaffold, 50 000 cells per dish were distributed. The cell culture medium was replaced every 2 days. Each well received 50 μL of the CCK-8 reagent (Promega, USA) after 1, 3, and 5 d, followed by incubation for up to 2 h. Following that, 96-well plates were used to transfer 100 μL of cell suspension from each well. Finally, a microplate reader (Sunrise Tecan, Australia) set to 450 nm was used to measure the absorbance in each well. After 3 days of cell culture, the morphology of the cells was further examined by LSM-510 (Carl-Zeiss, Germany) confocal microscopy using Rhodamine and DAPI (Molecular Probes, USA).[28,29] For live and dead assay, the MCF-7 cells were washed three times with PBS solution and stained with calcein and ethidium bromide, followed by incubation at RT for 10 min according to the manufacturer's protocol, before being checked by confocal microscopy.

2.7.2. *In vitro* anticancer study. MCF7 cell lines were seeded with a density of 50 000 cells into a 35 mm × 10 mm Petri dish with PCL (control sample), PCL–IONPs (PI) for hyperthermia alone, PDA for chemotherapy alone, and PIAD for the synergistic effect. All samples were taken in triplicate, then washed three times with PBS, and cultivated in Dulbecco's Modified Eagle Medium (DMEM, GIBCO) in a 5% CO_2 incubator at 37 °C in a humidified atmosphere. Cells grown on a coverslip were treated in triplicate with 5 g mL^{-1} Triton as a negative control. Following a 24 h incubation period, each sample received a warm PBS wash. After seeding the cancer cells, the AMF was turned on to investigate the effects of hyperthermia on the cells. To maintain the ideal temperature for hyperthermia, the magnetic field strength and frequency of the alternating magnetic field generator (OSH-120-B, OSUNG HITECH, Republic of Korea) were tuned to 12.57 kA m^{-1} and 293 kHz, respectively. Every 24 h, the medium was changed to maintain cultures. The PI, PIAD 0.5, and PIAD 1 nanofibers received hyperthermia treatment for 15 min in a sterile environment. After hyperthermia treatment of all samples, fresh DMEM was added and incubated in a 24-well plate again for 24 h in a 5% CO_2 incubator at 37 °C in a humidified environment, and then the CCK-8 reagent was added to each dish and incubated for 1–4 h according to the manufacture protocol. The absorbance at 450 nm was measured using a microplate reader. For further evaluation, live and dead cell assay was performed. For the assay, the MCF-7 cells were washed three times with PBS solution and stained with calcein and ethidium bromide, followed by incubation at RT for 10 min according to the manufacturer's protocol, before being checked by confocal microscopy. In addition, the morphology of the cells was observed using rhodamine and DAPI labeling (4′,6-diamidino-2-phenylindole, Thermo Fisher Scientific, Republic of Korea) to stain the cell-seeded scaffold. Confocal laser scanning microscopy was used to examine the cells (LSM 880, Carl Zeiss).

3. Results and discussion

3.1. Fabrication and characterization

The essential component of this drug carrier is ammonium bicarbonate (ABC), which may be integrated into electrospun fibers with an anticancer medicine *via* the electrospinning method. A previous study mentioned that in an acidic medium, ABC interacts with the acidic solution and quickly releases carbon dioxide (CO_2), which speeds up the release of drugs from the inner area of the fibers.[30] Simultaneously, ammonia is produced together with CO_2, which might counteract the tumor's acidic environment. As a result, PIAD electrospun nanofibers are considered a promising candidate for controlled drug delivery in anticancer applications.

As demonstrated in Fig. 1 and Table 1, various concentrations of ABC were effectively electrospun into PCL nanofibers loaded with IONPs. The SEM images of the prepared fibers in Fig. 1 indicate a typical smooth and bead-free morphology. Moreover, an increase of the ammonium bicarbonate concentration resulted in the darker red membrane of fibers.

Fig. 1A–C present a narrow size distribution of the nanofibers with the average fiber diameters of PCL, PIA 0.5, and PIA 1 calculated to be 0.442, 0.368, and 0.325 μm, respectively. It is possible that the amount of IONPs and ABC added to PCL solution plays a vital role in the effect on the viscosity of the electrospun fiber, which determines the flow rate in the needle, as well as the stability during the electrospinning process. In addition, Fig. 1F shows the TEM images of PIA nanofibers, which reveal the successful encapsulation of IONPs in the PCL–ABC fabricated nanofibers. Furthermore, the elemental analysis performed by EDX, as shown in Fig. 1D and E, indicates the presence of four elements (C, O, N, and Fe) in the PIA scaffold, with two characteristic peaks of IONPs. Meanwhile, further investigation of the PA 0.5 and PA 1 electrospun nanofibers was carried out (Fig. S1 of the ESI†), which showed well that only C, O, and N elements came from PCL and ABC. Therefore, it is confirmed that the fabrication of IONPs and ABC in the fiber is successful.

Fig. 2A displays the X-ray diffraction graph of the PCL, IONP, and PIA nanofiber samples. All diffraction peaks of the spectrum of the as-prepared IONPs agreed with the typical diffraction card, Joint Committee on Powder Diffraction Standard (JCPDS) No. 19–062. The crystalline plane with Miller indices of (311) is believed to be responsible for the main peak at 35.45°. Additional distinct peaks can be found, which correspond to the typical magnetite diffraction pattern at 30.10, 43.08, 53.45, 56.98, and 62.57° for the (220), (400), (422), (511), and (440) crystalline planes, respectively. Moreover, the presence of PCL in the PIA nanofiber is confirmed by the appearance of two sharp peaks at 2θ = 21.38 and 23.69°, which correspond to the (110) and (200) planes of the semi-crystalline PCL structure, in agreement with the literature.[31] It is also observed that the peaks from PIA become slightly wider and fainter, in comparison to those from pure PCL, implying low crystallinity and a smaller crystal size. For the PIA nanofibers, all characteristic peaks are the same as those of the IONPs, along with two typical crystalline peaks of PCL at 2θ = 21.73 and 24.13°, demonstrating that the IONPs are successfully integrated into the PCL fiber. Due to the low contents and embedded morphology underneath the composite nanofiber domain, the peaks relevant to ABC are difficult to discern. However, the presence of ABC is also supported by the FTIR spectrum of the PIA mat.

Fig. 2B shows the FTIR spectra of the IONPs, ABC, PCL, and PIA in the spectral range (400–4000) cm^{-1} to prove the distinctive bonding. In particular, the peak at 1007 cm^{-1} is due to the –C–OH stretching of HCO_3^-,[32] while the peaks at 1582 and 1164 cm^{-1} reveal the N–H bonding of ABC,[33] which show the natural characteristic vibration of ammonia belonging to NH_3 and N–H, respectively. Furthermore, absorption peaks appearing at 2945, 2867, 1721, 1295, 1240, 1164, and 1046 cm^{-1} for mats PCL and PIA are attributed to asymmetric and symmetric $-CH_2$ stretching, C═O stretching, C═C stretching, asymmetric and symmetric C–O–C stretching, and C–O stretching of PCL, respectively. The results also revealed that a broad peak

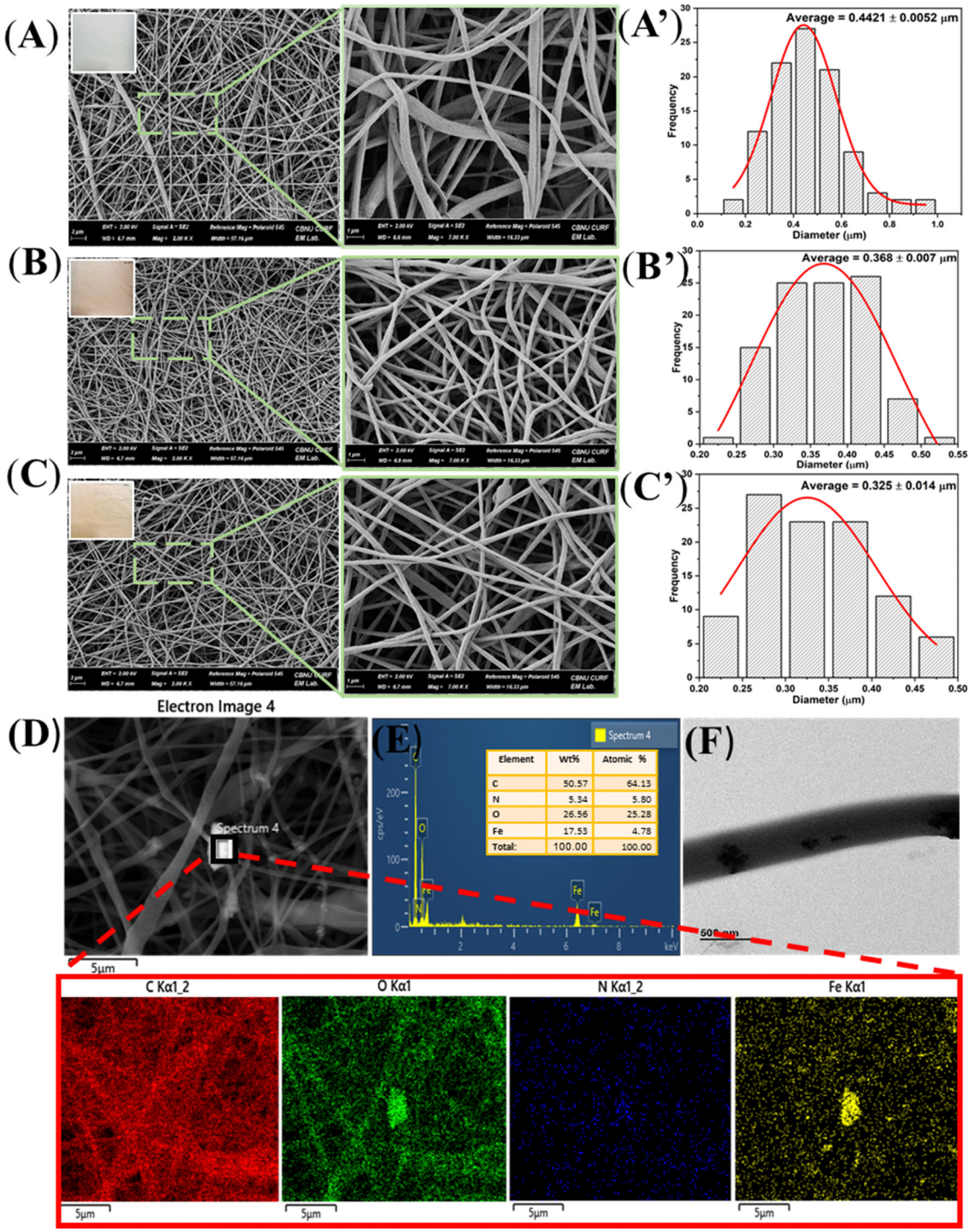

Fig. 1 FESEM images and the average diameters of different mats under different magnifications (A-A′) PCL, (B-B′) PIA 0.5, (C-C′) PIA 1; (D) and (E) the elemental content results obtained from EDX analysis and (F) TEM image of the PIA mat.

Table 1 Electrospinning parameters of the electrospun PIAD fibers

Sample	PCL (g)	IONPs (g)	DOX (g)	NH_4HCO_3 (mL)	Mean diameter (μm)
PCL	1	0	0	0	0.442 ± 0.005
PIAD 0.5	1	0.15	0.05	0.005	0.368 ± 0.007
PIAD 1	1	0.15	0.05	0.01	0.325 ± 0.014

at 581 cm^{-1} was present in the PIA fiber. This absorption peak may be a consequence of the newly created Fe–O linkages between the PCL and IONPs.[34] In essence, the FTIR spectrum of the PIA scaffold shows that following the electrospinning process, all the components retain their original chemical structures.

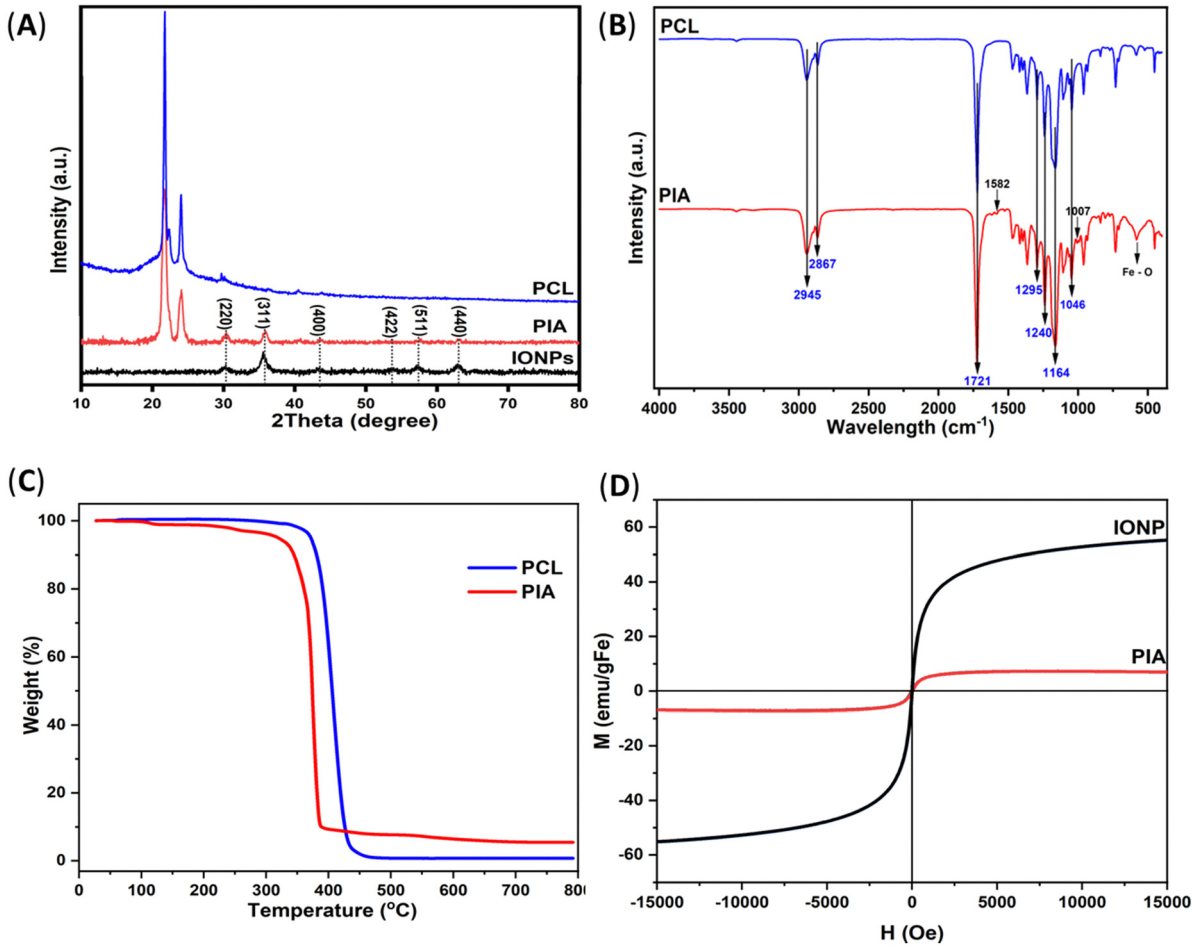

Fig. 2 XRD (A), FTIR (B), TGA (C) and VSM (D) analysis of PCL, IONPs and PIA fiber mats.

Fig. 2C shows that TGA was also carried out on the pure PCL and PIA nanofibers to study the impact of IONPs on the thermal stability of the nanocomposites, as well as the quantity of IONPs present in the sample. The trace indicates a steady weight loss up to 800 °C, with the initial step loss in the range 30–250 °C ascribed to the elimination of water and the substantial and abrupt weight loss of pure PCL happening in the range 300–425 °C attributable to the significant thermal degradation of the chains.[35] In contrast to the pure PCL, the degradation of the nanocomposites seems to occur in a lower temperature range. The most likely explanation is that the random pyrolysis of PCL chains caused by Fe_3O_4 nanoparticles results in the accelerated impact of IONPs on PCL thermal degradation.[36] Due to the presence of magnetic nanoparticles, the magnetized PCL fiber had a greater residue content at 450 °C than the non-magnetized PCL fiber.

The magnetic characteristics of the PCL fibers containing IONPs were assessed by measuring the hysteresis curve using a VSM approach (Fig. 2D). The magnetization curves of the IONPs and PIA did not exhibit a hysteresis loop, showing their superparamagnetic nature.[35] Magnetic fibers were found to have a saturation magnetization of 6.95 emu g^{-1}, which was lower than that of the pure IONPs determined at 55.17 emu g^{-1}. The high shape anisotropy of the fibers, as well as the presence of non-magnetic polymer PCL fibers around IONPs, may be responsible for the reduced magnetism of the magnetic fiber, when compared to the pure iron oxide nanoparticles, due to the negative impact on the performance of the magnetization expression. As a result, the IONPs and PIA with superparamagnetic properties are used in magnetic hyperthermia applications.

The surface wettability can affect drug release, because as the contact angle decreases, the wetting ability of the scaffold increases, leading to improved drug release,[37] similar to our previous study.[31] Hence, the surface wettability of the electrospun fibrous scaffolds plays a decisive role in the drug release, which is investigated in Fig. 3. The contact angle values of the electrospun PCL, PI, PIA 0.5, and PIA 1 fibrous scaffolds were 120, 87.4, 85.4, and 80.6°, respectively. The wettability of the composite nanofiber is enhanced slightly along with the incorporation of ABC and eventually changed from hydrophobic to hydrophilic, indicating that the PIA composite nanofibers are excellent for controlled drug release applications.

3.2. *In vitro* hyperthermia effect and drug release profile

Hyperthermia is typically used in such a multivalent oncological strategy in conjunction with other anti-cancer treatments, particularly when hyperthermia has been shown to generate a

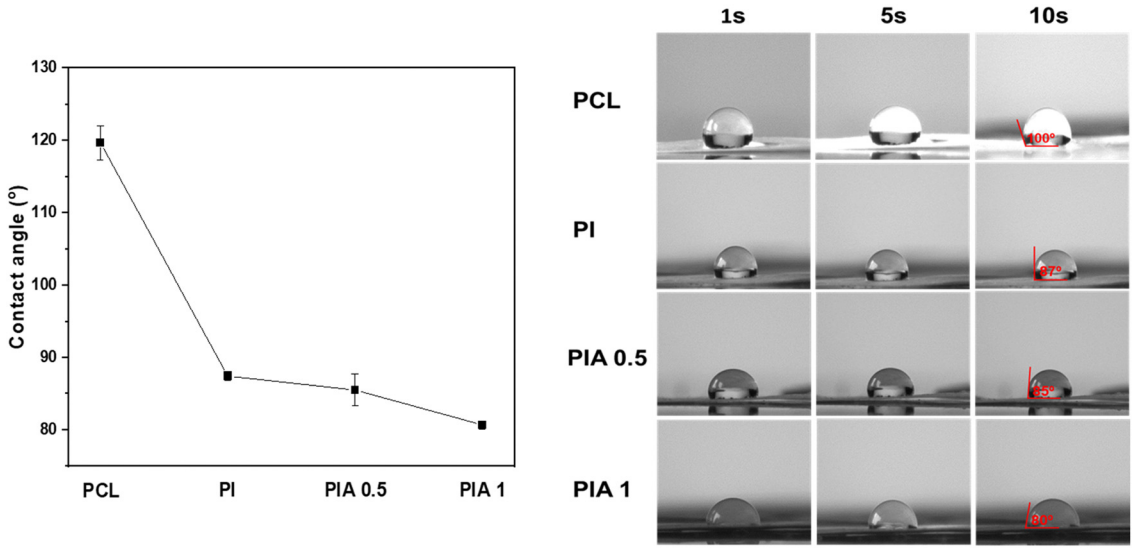

Fig. 3 Contact angle measurements of different samples in 10 s.

better synergistic effect. Indeed, when hyperthermia is administered at temperatures over 42 °C, tumor blood flow tends to diminish, but in normal tissue, it dramatically rises. Because of the slower rate of heat dissipation caused by the reduced blood flow, a tumor's temperature will rise more quickly than that of the surrounding normal tissue.[38]

For cancer hyperthermia treatment, PIA is extremely promising, because of its significant AMF responsiveness. Our previous study has revealed that, hyperthermia is identified as a crucial factor in cancer treatment, particularly in the context of breast tumors.[39] First, as shown in Fig. 4A, its hyperthermia capability was evaluated using an AMF generator. The magnetic hyperthermia properties of PIA with various IONP amount as well as IONPs were evaluated and displayed.

In the case of the PIA mat, the sample weights of 20, 40, and 60 mg showed temperature increases from 26 °C to 35.9, 41.8, 43.8, and 54.3 °C after 300 s. All PIA samples presented a rise in temperature during the excitation, and this temperature increase was accelerated with increasing PIA weight (Table 2); in contrast, the temperature of the control sample was not raised (Fig. 4A). It has been proven that after being maintained at 42 °C for 15 min, cancer cells can be destroyed and at temperatures of above 43 °C, with time diminished to 5 min, the cancer cells can be effectively killed.[40,41]

In contrast, PIA mat with 3 mg of IONPs (Table 2) only reached 35.9 °C and the same amount of bare IONPs reached above 80 °C. This could be explained by the relaxation loss, including Néel and Brownian relaxation, which is the main cause of the AMF-induced heating ability of IONPs with diameters smaller than 20 nm.[42] However, in the case of the PIA mat, as IONPs are fixed inside of the nanofibers, the complete rotation of the particles can be excluded, and so it is possible to rule out the complete rotation of the particles. As a result, Brownian relaxation has no effect on the magnetic heating that occurs. The heating caused by the magnetic reversal loss was only observed for fixed particles from the Néel losses and hysteresis losses.[43]

The PIA's hysteresis curve does not show coercivity or remanence. This suggests that during the magnetization reversal, the Néel losses are linked to the primary loss process. In the

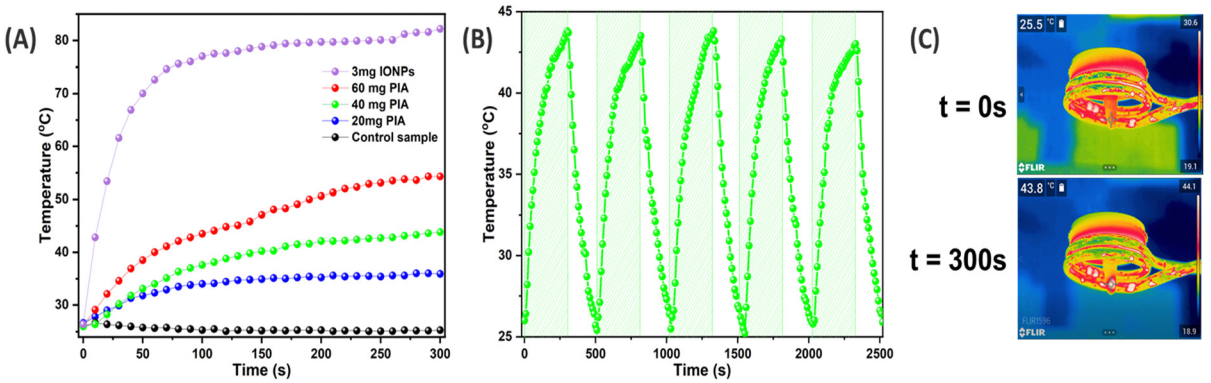

Fig. 4 Magnetic hyperthermia performance. (A) AMF-induced heating ability of IONPs and the PIA mat at different weights, (B) cyclic heating profile of PIA at 40 mg, and (C) thermographic images of the first cycle at 40 mg.

Table 2 Correlation between the weight of the PIA scaffold and the quantity of IONPs

Fiber weight (mg)	Respective amount of IONPs (mg)
20	3
40	6
60	9

case of cancer treatment, repeated heating for hyperthermia application is suggested, along with other therapeutic methods to diminish the risk of tumor metastasis.[44]

To examine the cyclic heating profile, 40 mg of PIA nanofibers was obtained in the presence and absence of an AMF (Fig. 4B). The results indicated that no difference in elevated temperature was observed throughout the entire cycle, making it a very stable system for the administration of hyperthermia therapy.[45]

3.3. *In vitro* drug release study

Fig. 5B shows the *in vitro* release profile results of DOX from the electrospun PD (PCL–DOX as a control sample), PIAD 0.5, and PIAD 1 fibrous scaffolds in pH 7.4 and 5.0 buffer solutions. Similar release behaviors were detected, and the total amounts of release for the PD, PIAD 0.5, and PIA 1 fibers were around 48.4, 49.9, and 56.25 μg mL^{-1}, respectively, during 120 h of incubation in pH 7.4 buffer solutions. This result showed that as expected, ABC did not affect the release of drug much at pH 7.4. In contrast, along with the increase in ABC concentration, there was a faster initial burst, and the total amounts of released DOX were higher in acidic medium.

Comparing the release profiles in pH 7.4 and 5.0 buffer solutions, the electrospun PCL fibrous scaffolds released approximately 71.5 μg mL^{-1} at pH 5.0, which is one and half times higher than the drug release amount at pH 7.4. These data showed that the intrusion of water into the polymer led to more degradation of the scaffold at pH 5.0 than that at pH 7.4.

Approximately 86 μg mL^{-1} DOX was released after 120 h from the PIA 0.5 scaffold at pH 5, 36 μg mL^{-1} higher than the amount released at pH 7.4, while PIAD 1 illustrated the drug release volume at a pH 5 of 103.9 μg mL^{-1}, almost twice as much as the drug release volume at neutral pH, with an initial burst of about 67.2 μg mL^{-1} in the first hour. Furthermore,

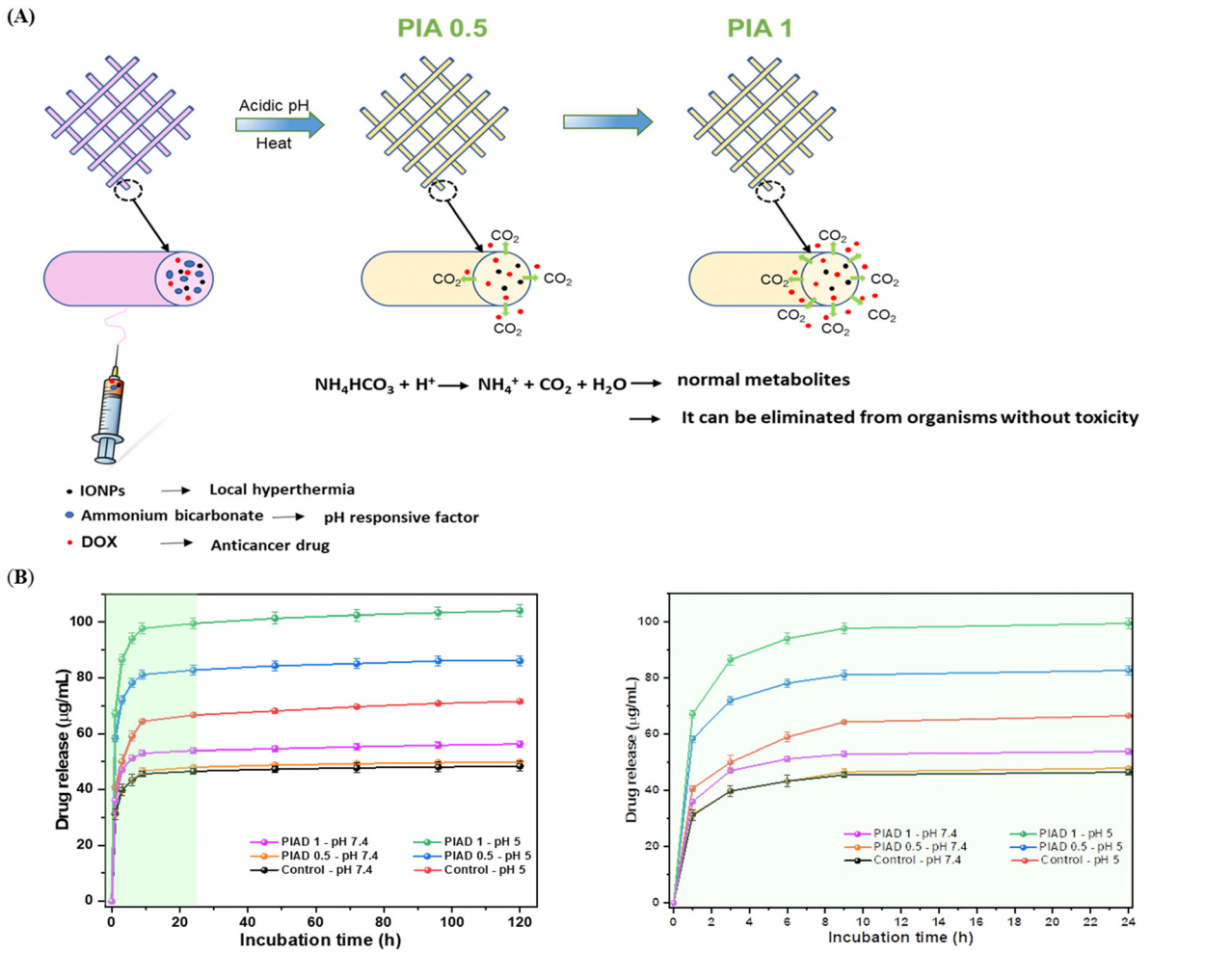

Fig. 5 Drug release properties. DOX release from the PIA mat in the acidic environment (A) and release profiles of DOX from the electrospun mat in PBS at pH 7.4 and pH 5 (B).

PIAD 1 shows drug release at pH 5 equal to 103.9 μg mL^{-1}, almost twice the drug release amount at pH 7.4, with an initial burst of about 67.2 μg mL^{-1} in the first hour. Jingwen Zhao *et al.* demonstrated a similar impact of sodium bicarbonate on drug release, exhibiting a consistent trend.[46]

For elucidating the intricacies of carbon dioxide production, Fig. S4 (ESI†) presents a portrayal of pH variations within the medium. The initial surge witnessed in the initial 48-hour period is attributed to the liberation of bicarbonate ions, serving as a buffering agent that consumes protons (H^+) and consequently results in a rise in pH. However, the subsequent decline in the medium's pH over time is construed as indicative of carbon dioxide production. Notably, the augmented presence of bubbles presumed to be CO_2 is perceptible in PIA 1 as opposed to PIA 0.5, particularly in an acidic environment (Fig. S4B, ESI†). This discrepancy substantiates the heightened efficacy of drug release from the PIA 1 sample in comparison to that from the PIA 0.5 sample, attributable to the greater release of CO_2. Furthermore, Fig. S4C (ESI†) reveals that even after a 120-hour incubation period at pH 5.0, the structural integrity of the fibers remains intact, although with a marginal degree of swelling observed in all fiber scaffolds. Consequently, these scaffolds emerge as viable substrates for the proliferation of normal cells post-treatment.

The impact of ABC may help to explain the high initial burst and responsive release profiles of DOX from PIA fibers. The ABC made the electrospun fibrous scaffolds more wettable, which encouraged water to enter the polymer block and facilitated the release of the loaded DOX from the fibers. Furthermore, ABC may have interacted with the acid after the acidic solution (pH 5.0) penetrated the polymer bulk, resulting in the production of CO_2 from the fibers, as well as the formation of ammonia, which may have neutralized the acid environment in the tumor (Fig. 5A).[47] In turn, this led to the loaded-DOX being released from the fibers and removed from the polymer bulk. The release profile indicated that, in an acidic environment, the fibers incorporated with ABC doubled the amount of drug released, compared to the control fiber in a neutral environment. Therefore, the drug release rate of DOX could be controlled in pH-responsive electrospun fibers through adjusting the content of ABC.

3.4. *In vitro* biocompatibility assay

NIH3T3E1 cells with the same density were seeded on different nanofibers, and the cell proliferation activities were measured using CCK-8 assay for 1, 3, and 5 d. None of the samples showed cytotoxicity. However, the cell viability test of PI and PIA shows significantly higher cell activities, compared to PCL group, which may be caused by the addition of IONPs, indicating the promoting effect of IONPs on the proliferation of NIH3T3E1, which may be related to the enhanced hydrophilicity after the addition of IONPs.

The cytoskeletal rhodamine B staining after 3 d shown in Fig. 6 reveals morphological differences of the NIH3T3 cells between the PCL, PI, and PIA samples and the growth patterns of the cells. PIA has better biological cell response, such as cell adhesion and proliferation, compared to PCL, in agreement with the CCK-8 results.

3.5. *In vitro* cytotoxicity assay

Cellular cytotoxicity of the prepared nanofibrous scaffolds was examined by the CCK-8 assay and live and dead assay studies. The MCF-7 cells were grown on the nanofibrous scaffolds for 24 h, and afterward they were treated with the AMF for 15.0 min, and then incubated for 24 h, followed by examining the toxicity and cellular uptake profile.

To reveal the individual and combined effects of hyperthermia and DOX on MCF-7 cells, the cells were divided into six groups: the cells in all the groups incubated with PCL (control), PCL containing IONP nanofibers (PI+) representing the hyperthermia group, the DOX-containing composite nanofibers (PIAD 0.5+), (PIAD 1+) representing the chemotherapy group or

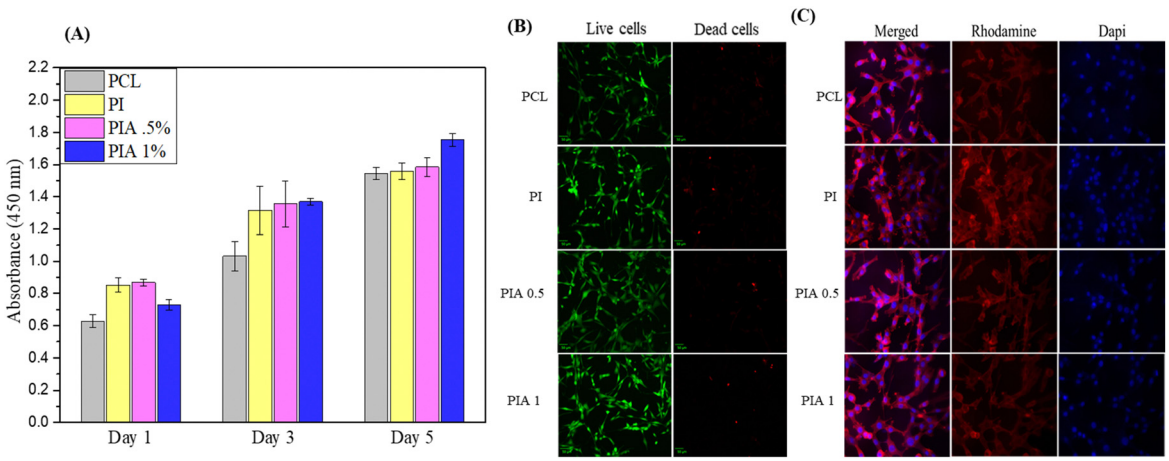

Fig. 6 *In vitro* biocompatibility evaluation of the scaffold. (A) Cell viability of different nanofiber samples after being cultured for 1, 3, and 5 days; (B) live/dead cell staining of NIH3T3 fibroblast cells on different scaffolds on day 5; (C) confocal microscopy images of rhodamine–phalloidin and DAPI-stained NIH3T3E1 cells after 5 days of culture. Nuclei and actin filaments were stained with DAPI (blue) and rhodamine (red), respectively. Rhodamine stains cytoskeleton, while DAPI stains the nucleus of cells. Scale bar represents 50 μm.

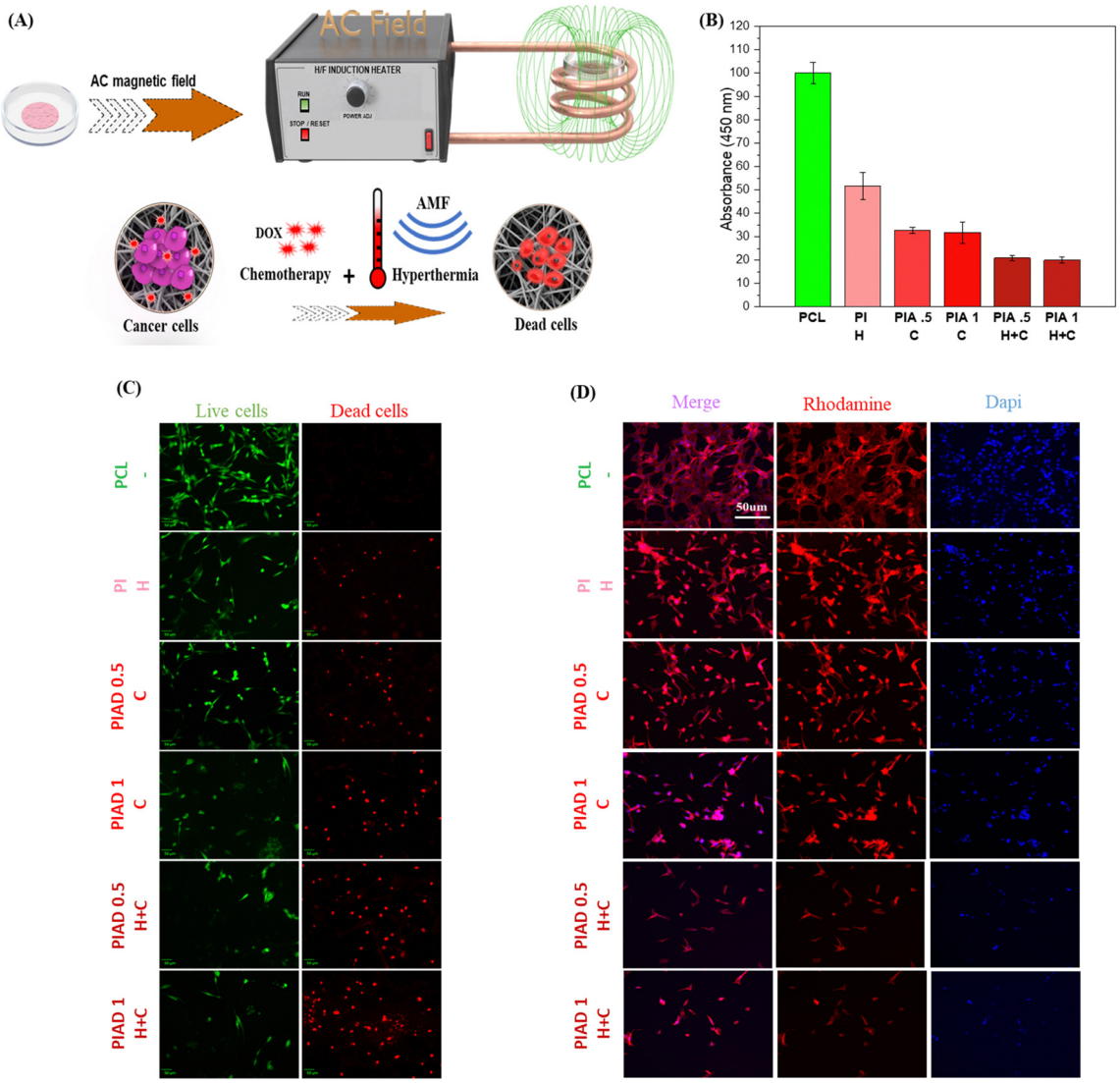

Fig. 7 *In vitro* cytotoxicity evaluation of the scaffold. (A) Cell viability of different nanofiber samples after different treatments; (B) live/dead cell staining of MCF-7 cells on different scaffolds on day 5; (C) confocal microscopy images of rhodamine–phalloidin and DAPI-stained NIH3T3E1 cells after 5 days of culture. Nuclei and actin filaments were stained with DAPI (blue) and rhodamine (red), respectively. Rhodamine stains cytoskeleton, while DAPI stains the nucleus of cells. Scale bar represents 50 μm; and (D) schematic illustration of the scaffold for hyperthermia induced by the AMF.

the hyperthermia and chemotherapy group (PIAD 0.5++), (PIAD 1++).

The viability test showed mild cytotoxicity (50%) against MCF-7 cells in the second group, when incubated with the fibrous mat (without Dox) and AMF-generated heat (PI+).

Similarly, the response of the third group of MCF-7 cells incubated with the DOX-containing fibrous mat (PIAD 0.5+), (PIAD1+) exhibited a significant reduction of cell viability different from the viability of the first group of cells. Furthermore, the cells incubated with the DOX-containing fibrous mat and AMF (PIAD 0.5++), (PIAD1++) exhibited remarkably reduced cell viability. This result suggests that the synergistic approach can lead to higher toxicity.

Furthermore, the results of CCK assay were further counter-checked with those of the confocal imaging technique using rhodamine–phalloidin and DAPI staining for qualitative evaluation (Fig. 7 D). The treated cells showed apoptosis features, such as blebbing of the nucleus and stunted actin growth.

The (PIAD 0.5++), (PIAD1++) group showed enhanced cell death due to the synergistic effect of DOX and hyperthermia, as the cytoskeleton was completely damaged, as compared to the (PI+) and (PIAD 0.5+), (PIAD1+) groups. The results show that PIAD is an ideal candidate for anticancer therapy by combining thermotherapy and chemotherapy to achieve enhanced apoptosis, due to the synergistic effect of DOX and hyperthermia.

Conclusion

The smart magnetic nanofiber scaffold has been successfully prepared by the incorporation of IONPs, ABC, and DOX into

PCL polymer solution through the electrospinning technique to achieve pH-sensitive DOX release. This study explained the pH-targeted delivery of DOX to MCF-7 cancer cells using ammonium bicarbonate (pH responsive factor), as well as the response to an alternating magnetic field to administer hyperthermia aided by IONPs, to reveal *in vitro* synergistic anticancer efficacy. Moreover, the *in vitro* cell culture test showed the high biocompatibility of PI and PIA, while PIAD++ showed enhanced cytotoxicity against MCF-7 cancer cells. This preliminary study showed that the pH-sensitive drug delivery properties of hyperthermic magnetic nanofibers might be beneficial for thermo-chemotherapy and the future development of new strategies for designing smart nanopatches, with the ability to control the release of the DOX anticancer drug to eradicate cancer cells.

Conflicts of interest

There are no conflicts to declare.

Acknowledgements

This work was supported by the grant of the Korea Health Technology R&D Project through the Korea Health Industry Development Institute (KHIDI), funded by the Ministry of Health & Welfare, Republic of Korea (grant number: HR22C1832). This research was also supported by the Basic Science Research Program through the National Research Foundation of Korea (NRF) funded by the Ministry of Education (NRF-2022R1I1A1A01064131) and the Brain Research Program of the National Research Foundation (NRF) funded by the Korean Government (MSIT) (NRF-2019M3C7A1032551, S.C.). We are thankful to CURF, Jeonbuk National University, South Korea for EDX mapping and XRD, FTIR, and FESEM spectroscopic analyses.

References

1 R. L. Siegel, *et al.*, Cancer statistics, *Ca-Cancer J. Clin.*, 2023, **73**(1), 17–48.
2 N. Dhas, *et al.*, Stimuli responsive and receptor targeted iron oxide based nanoplatforms for multimodal therapy and imaging of cancer: Conjugation chemistry and alternative therapeutic strategies, *J. Controlled Release*, 2021, **333**, 188–245.
3 Y. Xin, *et al.*, Nanoscale drug delivery for targeted chemotherapy, *Cancer Lett.*, 2016, **379**(1), 24–31.
4 H. Chen, *et al.*, Synergistic Chemotherapy and Photodynamic Therapy of Endophthalmitis Mediated by Zeolitic Imidazolate Framework-Based Drug Delivery Systems, *Small*, 2019, **15**(47), 1903880.
5 J. Khanom, *et al.*, Near-Infrared Responsive Synergistic Chemo-Phototherapy from Surface-Functionalized Poly (ε-caprolactone)–Poly (d, l-lactic-*co*-glycolic acid) Composite Nanofibers for Postsurgical Cancer Treatment, *Biomacromolecules*, 2022, **23**(9), 3582–3592.
6 L. Beola, *et al.*, Drug-Loaded Lipid Magnetic Nanoparticles for Combined Local Hyperthermia and Chemotherapy against Glioblastoma Multiforme, *ACS Nano*, 2023, **17**(18), 18441–18455.
7 D. Kai, S. S. Liow and X. J. Loh, Biodegradable polymers for electrospinning: Towards biomedical applications, *Mater. Sci. Eng., C*, 2014, **45**, 659–670.
8 L. J. Villarreal-Gómez, *et al.*, Electrospinning as a powerful technique for biomedical applications: a critically selected survey, *J. Biomater. Sci., Polym. Ed.*, 2016, **27**(2), 157–176.
9 A. I. Rezk, *et al.*, A Novel Design of Tri-Layer Membrane with Controlled Delivery of Paclitaxel and Anti-Biofilm Effect for Biliary Stent Applications, *Nanomaterials*, 2021, **11**(2), 486.
10 M. Laubach, P. Kobbe and D. W. Hutmacher, Biodegradable interbody cages for lumbar spine fusion: Current concepts and future directions, *Biomaterials*, 2022, 121699.
11 M. M. Zerankeshi, R. Bakhshi and R. Alizadeh, Polymer/metal composite 3D porous bone tissue engineering scaffolds fabricated by additive manufacturing techniques: A review, *Bioprinting*, 2022, e00191.
12 K. Shetty, A. Bhandari and K. S. Yadav, Nanoparticles incorporated in nanofibers using electrospinning: A novel nano-in-nano delivery system, *J. Controlled Release*, 2022, **350**, 421–434.
13 J. Park, Electroconductive Polythiophene Nanocomposite Fibrous Scaffolds for Enhanced Osteogenic Differentiation via Electrical Stimulation, *ACS Biomater. Sci. Eng.*, 2022, **8**(8), 1749–2143.
14 H. Mousa, Development of conductive polymeric nanofiber patches for cardiac tissue engineering application, *J. Appl. Polym. Sci.*, 2022, **139**(32), e52757.
15 E. Niiyama, *et al.*, Hyperthermia Nanofiber Platform Synergized by Sustained Release of Paclitaxel to Improve Antitumor Efficiency, *Adv. Healthcare Mater.*, 2019, **8**(13), 1900102.
16 Z. Li, J. Huang and J. Wu, pH-Sensitive nanogels for drug delivery in cancer therapy, *Biomater. Sci.*, 2021, **9**(3), 574–589.
17 F. Brero, *et al.*, Hadron therapy, magnetic nanoparticles and hyperthermia: A promising combined tool for pancreatic cancer treatment, *Nanomaterials*, 2020, **10**(10), 1919.
18 Y. Piñeiro, *et al.*, Iron Oxide Based Nanoparticles for Magnetic Hyperthermia Strategies in Biological Applications, *Eur. J. Inorg. Chem.*, 2015, (27), 4495–4509.
19 S. Nemec, *et al.*, Comparison of iron oxide nanoparticles in photothermia and magnetic hyperthermia: Effects of clustering and silica encapsulation on nanoparticles' heating yield, *Appl. Sci.*, 2020, **10**(20), 7322.
20 Y. H. Wang, *et al.*, Dually enhanced phototherapy by gambogic acid and hyperthemia-activated chemotherapy for synergistic breast cancer treatment, *Chem. Eng. J.*, 2023, 452.
21 M. Norouzi, *et al.*, Salinomycin-loaded nanofibers for glioblastoma therapy, *Sci. Rep.*, 2018, **8**(1), 9377.
22 H. Xing, *et al.*, Janus nanocarriers for magnetically targeted and hyperthermia-enhanced curcumin therapy of liver cancer, *RSC Adv.*, 2018, **8**(53), 30448–30454.

23 S. Shirvalilou, *et al.*, The future opportunities and remaining challenges in the application of nanoparticle-mediated hyperthermia combined with chemo-radiotherapy in cancer, *Wiley Interdiscip. Rev.: Nanomed. Nanobiotechnol.*, 2023, **15**(6), e1922.
24 F. Mohammad and N. A. Yusof, Doxorubicin-loaded magnetic gold nanoshells for a combination therapy of hyperthermia and drug delivery, *J. Colloid Interface Sci.*, 2014, **434**, 89–97.
25 L. L. Chen, *et al.*, A facile, flexible, and multifunctional thermo-chemotherapy system for customized treatment of drug-resistant breast cancer, *J. Controlled Release*, 2023, **363**, 550–561.
26 K.-J. Chen, *et al.*, A thermoresponsive bubble-generating liposomal system for triggering localized extracellular drug delivery, *ACS Nano*, 2013, **7**(1), 438–446.
27 M. H. Li, *et al.*, NIR-Activated Polydopamine-Coated Carrier-Free ''Nanobomb'' for In Situ On-Demand Drug Release, *Adv. Sci.*, 2018, **5**, 7.
28 J. W. Baek, *et al.*, Marine plankton exoskeleton-derived honeycombed hydroxyapatite bone granule for bone tissue engineering, *Mater. Des.*, 2022, **224**, 111372.
29 A. I. Rezk, *et al.*, De novo dual functional 3D scaffold using computational simulation with controlled drug release, *J. Colloid Interface Sci.*, 2022, **625**, 12–23.
30 X. Zhou, *et al.*, pH-Responsive and Recyclable Hydrogels for Gas Releasing and Scavenging, *Macromol. Rapid Commun.*, 2023, **44**(8), 2300008.
31 A. I. Rezk, *et al.*, Polyaniline-coated titanium oxide nanoparticles and simvastatin-loaded poly (ε-caprolactone) composite nanofibers scaffold for bone tissue regeneration application, *Colloids Surf., B*, 2020, **192**, 111007.
32 F. Milella and M. Mazzotti, Estimating speciation of aqueous ammonia solutions of ammonium bicarbonate: application of least squares methods to infrared spectra, *React. Chem. Eng.*, 2019, **4**(7), 1284–1302.
33 Z. Yu, *et al.*, Effect of Ammonium Bicarbonate on Intercalation and Exfoliation of Graphite Materials, *J. Nanomater.*, 2019, **2019**, 1–8.
34 S. Kumar, *et al.*, Magnetic field-guided orientation of carbon nanotubes through their conjugation with magnetic nanoparticles, *J. Mater. Sci.*, 2012, **47**, 1489–1496.
35 P. Ghaderinejad, *et al.*, An injectable anisotropic alginate hydrogel containing oriented fibers for nerve tissue engineering, *Chem. Eng. J.*, 2021, **420**, 130465.
36 G. Wang, *et al.*, Facile preparation of poly (ε-caprolactone)/Fe 3 O 4@ graphene oxide superparamagnetic nanocomposites, *Polym. Bull.*, 2013, **70**, 2359–2371.
37 H. A. Alhmoud and Y. H. Akkam, Combination of surfactants with other excipients: Effects on drug release and dimensional changes in matrices, *Trop. J. Pharm. Res.*, 2019, **18**(11), 2241–2246.
38 A. Hervault and N. T. K. Thanh, Magnetic nanoparticle-based therapeutic agents for thermo-chemotherapy treatment of cancer, *Nanoscale*, 2014, **6**(20), 11553–11573.
39 A. I. Rezk, *et al.*, Thermo-responsive-polymeric-gates of poly(N-isopropylacrylamide)/N-(hydroxymethyl)acrylamide coated magnetic nanoparticles as a synergistic approach to cancer therapy: Drug release and kinetics models of chemothermal magnetic nanoparticles, *Mater. Des.*, 2023, 234.
40 R. W. Y. Habash, *et al.*, *Thermal Therapy*, Part 1: An Introduction to *Thermal Therapy*. 2006. **34**(6): 459–489.
41 Y. Liu, *et al.*, Dopamine-Melanin Colloidal Nanospheres: An Efficient Near-Infrared Photothermal Therapeutic Agent for In Vivo Cancer Therapy, *Adv. Mater.*, 2013, **25**(9), 1353–1359.
42 S.-h Noh, *et al.*, Nanoscale magnetism control via surface and exchange anisotropy for optimized ferrimagnetic hysteresis, *Nano Lett.*, 2012, **12**(7), 3716–3721.
43 C. L. Dennis and R. Ivkov, Physics of heat generation using magnetic nanoparticles for hyperthermia, *Int. J. Hyperthermia*, 2013, **29**(8), 715–729.
44 P. Wust, *et al.*, Hyperthermia in combined treatment of cancer, *Lancet Oncol.*, 2002, **3**(8), 487–497.
45 A. GhavamiNejad, *et al.*, Mussel-Inspired Electrospun Smart Magnetic Nanofibers for Hyperthermic Chemotherapy, *Adv. Funct. Mater.*, 2015, **25**(19), 2867–2875.
46 J. W. Zhao, *et al.*, Smart electrospun fibrous scaffolds inhibit tumor cells and promote normal cell proliferation, *RSC Adv.*, 2014, **4**(93), 51696–51702.
47 D. Banerjee and S. Bose, Comparative effects of controlled release of sodium bicarbonate and doxorubicin on osteoblast and osteosarcoma cell viability, *Mater. Today Chem.*, 2019, **12**, 200–208.